J. Fluid Mech. (1996), vol. 307, pp. 269–296

Convection in ^{3}He–superfluid-^{4}He mixtures. Part 1. A Boussinesq analogue

By GUY METCALFE[1] AND R. P. BEHRINGER[2]

[1]Division of Building, Construction and Engineering, CSIRO, Highett 3190, Australia

[2]Duke University Department of Physics and Center for Nonlinear and Complex Systems, Durham, NC 27708, USA

(Received 13 October, 1994 and in revised form 20 September 1995)

Dilute mixtures of ^{3}He in superfluid ^{4}He have Prandtl numbers easily tunable between those of liquid metals and water: $0.04 < Pr < 2$. Moreover, owing to the tight coupling of the temperature and concentration fields, superfluid mixture convection is closely analogous to classical Rayleigh–Bénard convection, i.e. superfluid mixtures convect as if they were classical, single-component fluids, well described by the Boussinesq equations. This work has two goals. The first is to put the theory of superfluid mixture convection on a firmer basis. We accomplish this by combining experiment and analysis to measure superfluid effects on the onset of convection. In the process, we demonstrate quantitative control over superfluid effects and, in particular, that deviations from classical convective behaviour can be made small or at worst no larger than finite aspect ratio effects. The size of superfluid effects at convective onset can be less than a few percent for temperatures $1 < T < 2$ K. Comparison of the measured properties of superfluid mixture roll instabilities above the onset of convection (e.g. skewed varicose, oscillatory, and particularly near the codimension-2 point) to the properties predicted by Boussinesq calculations further verifies that superfluid mixtures convect as classical fluids.

With superfluid effects understood and under control, the second goal, presented in Part 2, is to exploit the unique Pr range of superfluid mixtures and the variable aspect ratio (Γ) capabilities of our experiment to survey convective instabilities in the broad, and heretofore largely unexplored, parameter space $0.12 < Pr < 1.4$ and $2 < \Gamma < 95$. The aim is to identify and characterize time-dependence and chaos, and to discover new dynamical behaviour in strongly nonlinear convective flows.

1. Introduction

Rayleigh–Bénard convection (RBC), convection in a horizontal layer of fluid subject to a destabilizing density gradient, has become a prototypical experiment for the study of dynamical systems undergoing both linear and nonlinear instabilities. Superfluid mixture convection (SMC) is an analogous but much less studied form of convection that occurs when an adverse density gradient is created in a horizontal layer of a dilute mixture of ^{3}He in superfluid ^{4}He. An important motivation for using such a novel fluid is the remarkable Prandtl number range available with superfluid mixtures – $0.04 < Pr < 2$. Over this range the dynamics of RBC rolls is expected to vary dramatically, but no conventional fluid spans this range. For instance, liquid metals lie at the lowest Prandtl numbers, gases near $Pr = 0.7$, and water or

other dense fluids roughly above $Pr = 2$. This Pr range gives SMC the potential to be an extremely valuable tool for understanding convective flows by expanding the experimental parameter space to areas that previously could only be studied theoretically.

However, it is not obvious that experiments on SMC should be directly related to calculations for RBC that explicitly assume a classical single-component fluid. Nominally, superfluids have very different properties from classical fluids, and ordinary binary mixtures show very different convective states from classical single-component fluids. Nonetheless, we present analytical and experimental evidence to demonstrate that convecting superfluid mixtures behave analogously to single-component classically convecting liquids. For a broad range of conditions we are able to quantify and control the deviations of SMC from RBC and show that these deviations can be made negligibly small.

The goals of this work are twofold: first, to test with both experiment and theory the analogy between RBC and SMC; second, in Part 2 (Metcalfe & Behringer 1996), to survey new convective instabilities and behaviour in the enlarged parameter space available with SMC. In the remainder of the introduction we briefly review relevant features of RBC and SMC. Much of this work involves a novel cryogenic apparatus that we describe in §2. In §3 we consider the equations of motion for SMC and show the results of experiments used to quantify differences between RBC and SMC near the onset of convection. Section 4 presents further data investigating nonlinear roll instabilities, in particular near the predicted codimension-2 point. We summarize the results of Part 1 in §5.

1.1. *Control parameters and response variables*

To streamline the subsequent presentation, we define several essential terms in this section. Relevant control parameters are the Rayleigh and Prandtl numbers and a roll wavevector, defined respectively as

$$Ra = \frac{|\alpha_{P,\mu_4}|\, g d^3 \Delta T}{\nu \chi_{eff}}, \tag{1.1}$$

$$Pr = \frac{\nu_n}{\chi_{eff}}, \tag{1.2}$$

$$q = \frac{2\pi d}{\lambda}. \tag{1.3}$$

Here ΔT is the temperature difference across a fluid layer of height d; the fluid parameters, α_{P,μ_4}, χ_{eff} and ν are respectively the expansion coefficient at constant pressure and ^{4}He chemical potential μ_4, an effective thermal diffusivity, as defined in Fetter (1982*a*, *b*), and the kinematic viscosity; g is the acceleration due to gravity; $\nu_n = (\rho/\rho_n)\nu$, where ρ and ρ_n are respectively the total and normal fluid densities. Specifically, χ_{eff} is constructed from the effective thermal conductivity κ_{eff} and an appropriate specific heat. The conductivity is 'effective' because in these mixtures heat flow consists of an ordinary diffusive component and a component associated with superfluid flow – both of which are proportional to the temperature gradient. Also, λ is the wavelength of the convection pattern, or alternatively, the length of a pair of convection rolls.

Many calculations assume a horizontally infinite fluid layer, but for an experiment, the value of q is set (at onset) in response to the fluid container size and the third important control parameter becomes the aspect ratio of the convection cell

$$\Gamma = \frac{l_x}{d}, \tag{1.4}$$

where l_x is the length of the long side of a rectangular convection cell. At onset, assuming straight parallel rolls, an integral number of rolls must fit into l_x: $n\lambda/2 = l_x$, where n is the number of rolls. Thus, the critical wavevector at the onset of convection $q_c = n\pi/\Gamma$. For rigid boundaries the expected critical wavevector in the infinite-Γ limit is $q_{co} \approx \pi$, so that

$$q_c \approx nq_{co}/\Gamma. \tag{1.5}$$

Since rolls typically come in pairs, whenever Γ is an even integer, we expect rolls with the critical wavevector q_{co}. However, it should be kept in mind that q_c is not under strict experimental control. Although a variable-Γ cell allows more control than a fixed-Γ cell, cryogenic convection studies cannot at this time visualize flows in order to directly measure q_c. Without direct visualization we may strictly only talk about the most likely pattern scenarios, and then compare where possible against room temperature visualization experiments and/or calculations of the dimensionless heat transport or Nusselt number based on specific patterns. It is precise to say that we have reproducible experimental influence over q_c through the variability of Γ.

Ra, *Pr* and Γ form the experimental control parameter space. We measure the response of the fluid to changes in these parameters through the Nusselt number

$$N = \frac{C_{h(total)}}{C_{h(preconvective)}}, \tag{1.6}$$

where C_h is the thermal conductance of the fluid layer. $N - 1$ measures the scaled amount of heat carried by convective motion alone.

1.2. *Instabilities of convection rolls*

Study of RBC was relatively sparse until the 1970s which saw a rapid increase in not only the study of RBC but more broadly of pattern-forming systems and even more broadly of nonlinear dynamical systems (Cross & Hohenberg 1993).

The initial instability of RBC is from an isotropic conduction state to an arrangement of rolls. Generally speaking, the initial roll pattern is forced by the sidewalls and ideally in a rectangular cell the rolls are straight, parallel and aligned with the short side of the cell. This means that the rolls are effectively one-dimensional, the roll amplitude being the only responsive variable. Past the regime of effectively one-dimensional straight parallel rolls lie transitions to complex temporal and spatiotemporal behaviour. In order to understand these very complicated flows, one would like to know how they arise: to know the full range of instabilities which destroy the simple one-dimensional pattern of rolls. Clever & Busse (1974, 1979, 1987) have calculated the stability boundaries in *Ra*–*Pr*–*q* space of straight parallel rolls assuming an infinite aspect ratio. The three-dimensional region of stability of straight rolls is often referred to as the Busse balloon (Busse 1981).

When experiments in large aspect ratio containers (say $\Gamma \sim 30$) take care to promote straight rolls, the quantitative agreement with calculations is excellent (Croquette 1989*a*, *b*). In small-Γ cells, the measured instability boundaries are systematically shifted up in *Ra* but qualitative agreement with the calculations remains. As *Ra* is raised, rolls may not remain parallel but may bend and nucleate defects.

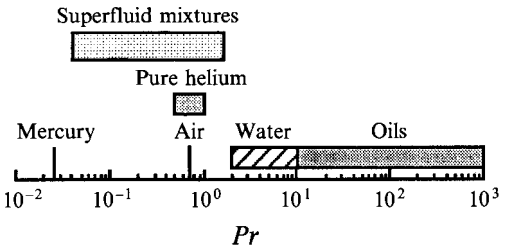

FIGURE 1. Illustration of the Pr range of fluids commonly used in experiments. Of particular relevance is the large gap in Pr between water and liquid metals (represented by mercury) that is bridged by superfluid mixtures.

Roll bending leads to mean flows on length scales the size of the container. These mean flows can strongly affect the stability of the roll pattern. Roll curvature effects require additional analysis (Newell, Passot & Souli 1990) and are not taken into account by the infinite-Γ stability calculations. It is beyond our scope to go into further details. Any of a number of recent reviews and books summarize results to date, for example those by Behringer (1985), Ahlers (1989), Manneville (1990), or Cross & Hohenberg (1993).

Two general types of instability occur at the boundaries of the region of roll stability (see figure 12): stationary pattern changing instabilities, such as the skewed varicose, which act to keep the pattern within the stable band of wavenumbers; and time-dependent instabilities, such as the oscillatory instability. A fluid which could be continuously tuned to take on both of these instability types, while keeping $q = q_c$, would be very useful for the study of nonlinear instabilities.

1.3. *Prandtl number gap*

To initiate the oscillatory or the skewed-varicose instability in a constant experimental setting, while keeping $q = q_c$, requires a fluid with a Prandtl number tunable between about 0.03 and 0.7. No common fluid (figure 1) has such a range of Pr. Water, liquid metals, pure ^{3}He or ^{4}He, and all gases fall in or near this range of Pr, but do not cover it fully and specifically do not cover it enough to be able to change which instabilities occur after the onset of convection.

To our knowledge, superfluid mixtures are the only fluids to provide a tunable Prandtl number of broad enough range to access the change from stationary to time-dependent instabilities. Figure 2 shows the Prandtl number of the dilute mixture used in our experiments as a function of temperature along with Pr for several other cryogenic fluids for comparison. Wheatley and coworkers (Warkentin *et al.* 1980; Haucke *et al.* 1981) first recognized that dilute superfluid mixtures bridge this Prandtl number gap.

1.4. *Buoyant instability of superfluid mixtures*

For RBC the buoyancy mechanism is well known. The fluid layer is heated from below; hot fluid becomes less dense than the overhead cold fluid and a density inversion is born, which, if large enough to overcome dissipative forces, leads to bulk overturning motion in the fluid. For SMC the buoyancy mechanism is more complex. In *pure* superfluid ^{4}He it is impossible to create a thermal gradient (with moderate heat fluxes) and hence impossible to create a density inversion. However, small additions of ^{3}He allow dilute superfluid mixtures to sustain a density inversion through the 'heat-flush' effect that concentrates lighter ^{3}He atoms at the cold side of

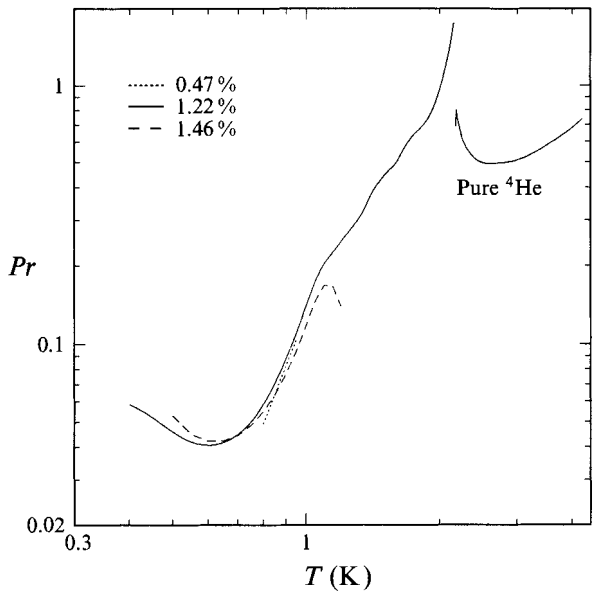

FIGURE 2. The Prandtl number of several cryogenic fluids versus temperature on log-log scales. The solid line shows *Pr* for the 1.22% ^{3}He–superfluid-^{4}He mixture used throughout this work. The dashed lines show *Pr* reported for other mixture concentrations (Warkentin *et al.* 1980). For comparison, *Pr* for pure ^{4}He is displayed; also of note is that the minimum *Pr* for pure ^{3}He is 0.5. All data are at saturated vapour pressure. We believe the maximum in *Pr* for the 1.46% data is probably an artifact of the sparse and inexact thermo-hydrodynamic data generally available for dilute superfluid mixtures in this temperature range. Extensive data for the 1.22% mixture are available from the authors or the JFM Editorial Office.

the cell (Khalatnikov 1965). This effect creates dissipation and allows the creation of a thermal gradient.

The dynamics of superfluids is expressed by the two fluid-model (Landau 1941; London 1954; Khalatnikov 1965). In this description, the liquid consists of two separate components, normal and superfluid, each with its own density ρ_n and ρ_s, and velocity $\boldsymbol{v}_n$ and $\boldsymbol{v}_s$, respectively. The total mass flux is given by

$$\boldsymbol{j} = \rho_n \boldsymbol{v}_n + \rho_s \boldsymbol{v}_s. \tag{1.7}$$

The normal fluid is to be thought of as a conventional viscous fluid, but the superfluid has neither viscosity nor entropy. In the case of pure superfluid ^{4}He, heat flow takes place without dissipation by 'counterflow'. Thermal energy is carried from a source to a sink by a flow of normal fluid. At the sink, the normal fluid converts to superfluid which returns without dissipation to the source. Dissipationless counterflow enforces the condition $\nabla \mu_4 = 0$.

The addition of ^{3}He to the superfluid ^{4}He leads to a substantially different process. The ^{3}He atoms are part of the normal fluid and participate in the thermal transport of energy from source to sink. But, unlike the ^{4}He, the ^{3}He atoms are not superfluid (at these temperatures) and so cannot participate in the superfluid counterflow; the heat flow flushes ^{3}He to the cold side producing a gradient in the ^{3}He mass concentration c. The resultant mass flux along ∇c is a dissipative flow. Thus, in the absence of a

pressure gradient (essentially the case here), the temperature gradient ∇T is linearly related to ∇c:

$$\nabla c = -(k_T^*/T)\nabla T. \tag{1.8}$$

The quantity k_T^*, the effective thermal diffusion ratio, takes its name in analogy to the ordinary thermal diffusion ratio k_T which appears in the diffusive impurity current

$$\boldsymbol{i} = -\rho\mathscr{D}\left(\nabla c + (k_T/T)\nabla T\right), \tag{1.9}$$

where $\boldsymbol{i}$ is the impurity flux of ^{3}He atoms and $\mathscr{D}$ is the ^{3}He mass diffusion coefficient. Unlike the ordinary thermal diffusion ratio k_T, which is a transport coefficient, k_T^* is a thermodynamic quantity relating changes in c and T under conditions of constant chemical potential μ_4 and pressure P:

$$k_T^* \equiv -T(\partial c/\partial T)_{P,\mu_4}. \tag{1.10}$$

Consequently, the fluid behaves as a pure fluid with an effective thermal expansion coefficient

$$\alpha_{P,\mu_4} = -\rho^{-1}(\partial\rho/\partial T)_{P,\mu_4} \tag{1.11}$$

that is always negative. This means that convection is initiated by heating from above rather than from below. In the more general dynamical case, neither μ_4 nor P need be constant. The important criterion is whether the speed of the convective flow is much slower than the velocity of second sound (a propagating thermal mode of the superfluid equations). As this is almost always the case for superfluid convection, the condition that μ_4 be constant is typically satisfied.

To the extent that (1.8) is a good approximation, c is slaved to T. This slaving is the reason that superfluid mixtures convect analogously to single-component fluids, rather than as binary mixtures. If c and T are slaved, there is effectively only one scalar field in the problem. Of course, the full dynamical equations of SMC differ from ordinary RBC. For instance, the appropriate mass current is given by (1.7) with the consequence that for incompressible flow $\nabla\cdot\boldsymbol{v}_n \neq 0$. Superfluids also have extra dissipative processes characterized by several generalized viscosity coefficients (second viscosities) which have no analogue in RBC. These effects, though, in most instances turn out to be small and can be considered as superfluid perturbations to RBC. Section 3 examines in some detail the effects of additional superfluid terms in (1.8).

2. Experimental apparatus and techniques

The goals of this work are to assess the extent of the analogy between RBC and SMC and to survey convective instabilities in the $Ra - Pr - \Gamma$ parameter space. The central tool used to accomplish these goals is the variable-height convection cell and accompanying cryogenic system described in this section. The unique feature of this apparatus is that it allows us to continuously vary the height (and hence aspect ratio) of the fluid layer while the rest of the apparatus and sample fluid remain unchanged and at low temperature. The cryostat is similar in principle to that used by Gao *et al.* (1987) to study convection in non-superfluid ^{4}He and ^{3}He–^{4}He mixtures. However, the use of superfluid mixtures required an entirely new apparatus (in order to heat from above). Metcalfe (1991) has additional experimental details.

The chief reason for using cryogenic techniques is to take advantage of the unique Pr range of dilute superfluid mixtures. Beyond this, the cryogenic environment offers other benefits to convection research, as described in more detail

by Ahlers (1974), Ahlers (1975) and by Behringer (1985). Temperature measurements with very high stability and resolution are possible. For the measurement of heat flow and temperature gradients, it is standard to resolve temperature changes $\Delta T/T \sim 10^{-6}$. The cryogenic environment is unmatched for detecting time-varying thermal signals. This is due to the large ratio of the heat capacities of cryogenic fluids to the metal bounding plates. The heat capacity ratio for equal volumes of fluid and copper is $\sim 10^3$ for liquid helium, ~ 1 for water, and $\sim 10^{-2}$ for pressurized room temperature gases. Consequently, cryogenic experiments are unmatched at identifying time-dependence in thermal signals.

The disadvantage of liquid helium experiments is the difficulty of imaging the flow patterns, although the advantages of precision and versatility can be exploited to provide extensive information on convective flows. Behringer's (1985) review particularly emphasizes results obtained from cryogenic convection studies. In addition, Sullivan, Ecke & Steinberg (1991) have recently calculated that shadowgraph techniques should have adequate sensitivity to visualize the convective flows in superfluid mixtures.

2.1. *Cooling and cryostats*

The cryogenic part of the apparatus is sealed inside an evacuated can and immersed in liquid helium at 4.2 K. Cooling below 4.2 K is provided by two helium evaporation refrigerators. The first is a continuously operating ^{4}He refrigerator (Delong, Symko & Wheatley 1971). The second recirculates ^{3}He in a closed cycle. Each refrigerator's liquid capacity is about 8 cm^3. The minimum loaded temperature with these refrigerators is ≈ 0.8 K. For temperatures below ≈ 1.3 K, the ^{4}He refrigerator's function is to condense returning ^{3}He gas. Below the ^{3}He refrigerator is an isothermal platform, intended as a buffer between the refrigerators and sample chamber, and below that the combined sample chamber and convection cell.

The refrigerators, the isothermal platform, and the sample chamber are connected serially by heat leaks that are chosen to extract the heat injected to drive convection without directly linking the refrigerators to the convection cell. This design allows us to easily change the temperature $T_\circ$ at the bottom of the convection layer without adjusting the refrigerators. $T_\circ$ is regulated by changing the voltage across resistive heaters on the sample chamber and isothermal platform. In practice, applying regulating heat only to the isothermal platform provided superior temperature regulation at the sample chamber.

2.2. *Sample chamber, convection cell, and piston*

The heart of the apparatus consists of the sample chamber, convection cell, and height-changing piston (figure 3). The sample chamber provides a liquid reservoir and a large thermal mass at the constant-temperature side of the convection layer. It consists of two copper cylinders indium-sealed together. The entire vessel is 2.86 cm tall with a 6.99 cm diameter. The interior of the sample chamber is honeycombed with a large number of holes, producing a net interior volume of about 10 cm^3.

The convection cell is mechanically and thermally connected directly to the top of the sample chamber. The convection cell has a rectangular cross-section of length $l_x = 2.284$ cm and width $l_y = 1.013$ cm, giving a cross-sectional area of 2.314 cm^2. The sidewalls are a stainless steel rectangular tube of wall thickness 0.264 mm, giving a wall cross-sectional area of 0.1771 cm^2. This tube is soldered at each end to annular copper blocks which surround the tube. An additional copper block which forms the top plate of the convection apparatus fits inside the stainless steel tube and is secured with screws and epoxy to the upper annular copper block. This construction

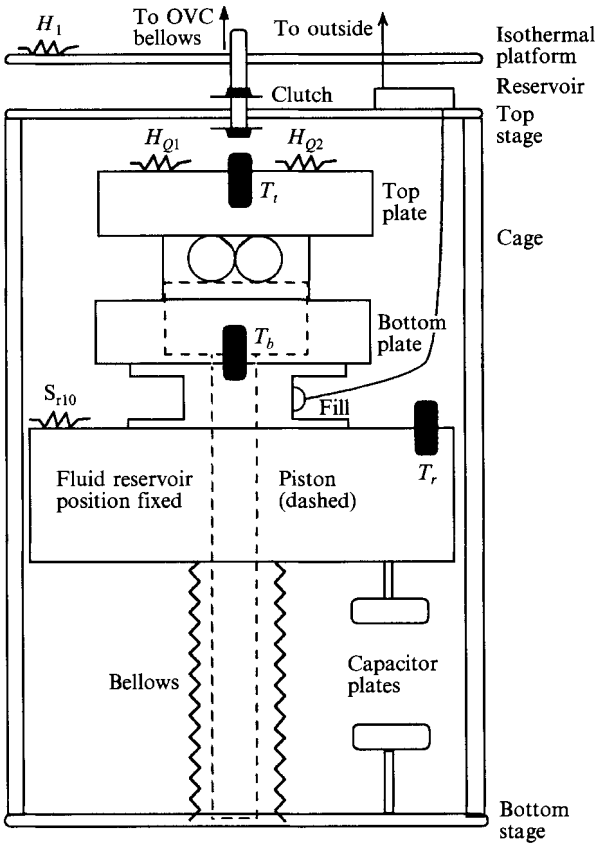

FIGURE 3. Sketch of the sample chamber and convection cell (not to size); and the schematic location of heaters and thermometers. The height-changing piston is drawn with a dotted line. For clarity the middle stage of the cell cage, the thermal anchoring clamps, and the top variable capacitor are not pictured.

is used to guarantee that there are no temperature gradients between the sidewalls and the upper boundary of the fluid at their juncture. The lower annular copper block is indium-sealed to the top of the sample reservoir. The top and bottom copper confining plates are polished to a reflecting finish. Both plates are flat to a few wavelengths, as measured by an optical flat and a sodium vapour light source. The upper plate is fixed in position while the lower plate is the top of a piston. The piston fits snugly against the sidewalls with a mean gap between the walls and the piston that we estimate to be about 10 μm. The space between the upper surface of the piston and the upper bounding plate forms the convection region. Sample fluid enters the convection region by welling up from the sample chamber through the gap between the sidewalls and piston head. The convection cell height d is continuously adjustable from 1.006 cm to 0 (top and bottom plates touching) by varying the position of the piston in the cell. The shaft of the bottom plate piston passes completely through the sample chamber. A beryllium copper bellows is soft soldered to the bottom of the sample chamber.

The final feature of the sample chamber/convection cell is a small fluid reservoir located a few centimetres above the top of the convection cell. The reservoir is also honeycombed internally with many small holes. In operation, the liquid–vapour

interface sits within the reservoir to ensure that fluid in the convection cell is at saturated vapour pressure. The 2 cm^3 reservoir is connected to the sample chamber by a 1.6 mm o.d. copper capillary; the reservoir is at the sample chamber temperature. A 1.6 mm o.d. $\times$ 0.25 mm wall stainless steel capillary leads from the reservoir to the sample tanks outside the dewar.

Note two important features in the construction of the sample chamber/convection cell: (i) the convection layer can be heated from above, as required by the negative thermal expansion coefficient; and (ii) the movable piston allows *in situ* change of the height of the convection cell.

2.3. *Preparation and analysis of the mixture*

Sample mixture fills the sample chamber, bellows, and convection cell, as well as partially filling the fluid reservoir. The total sample volume is about 25 cm^3, which is filled with a little over 0.9 moles of dilute ^{3}He–^{4}He mixture. The ^{3}He–^{4}He mixture was prepared by combining pure ^{4}He and ^{3}He gas at room temperature and then condensing the gas into the sample chamber at low temperatures. A mole count of the helium gases gives the mole fraction of the mixture as $X = 0.0122$. T_λ for the mixture was found to be 2.1554 K, which implies a mole fraction $X = 0.0120$. These independent measures substantially agree and we take the mole fraction of our mixture to be $X = 0.0122$ (mass fraction $c = 0.00922$).

2.4. *Changing the cell height*

The height of the cell is changed while at helium temperatures by turning a finely pitched screw on top of the dewar that in turn pushes or pulls the piston whose head is the bottom plate of the convection cell. The screw is attached to a stainless steel tube running from the top of the cryostat through the liquid helium bath to a bellows seal at the top of the vacuum can. This bellows mechanically links another stainless steel tube running though the vacuum can to a 'cage' around the sample chamber/convection cell assembly (figure 3). The cage is rigid and consists of three copper stages connected by copper posts; the stages each have differently shaped central cutouts. (For clarity the middle stage of the cage is not pictured in figure 3.) The copper cage stays at the sample chamber temperature. The piston and cage move rigidly through the action of the pushrod compressing (expanding) the bellows to decrease (increase) the cell height. Friction holds the piston in place. The height is easy to change but once set is very stable.

The mechanical structure of the cage serves two purposes. First, a direct mechanical (and hence thermal) connection of the pushrod to the convection cell is undesirable. Consequently, the top of the cage is a clutch mechanism. When taking measurements, the pushrod is physically (and thermally) disconnected from the sample chamber/convection cell. The clutch is engaged only when actually changing the height. Second, there are spring-loaded clamps mounted on the middle stage that press snugly against the outside of the stainless steel wall at a level which is nearly at, but slightly below, the upper surface of the piston. These pieces help thermally anchor the bottom outer part of the stainless steel wall at the sample chamber temperature and also help keep the piston from slipping when the clutch is disengaged. The clamps travel with the cage and so keep level with the bottom plate through all changes of cell height. Two sets of capacitor plates are attached to the cage and sample chamber. These capacitors yield a precise measurement of the cell height.

2.5. *Measurement electronics and calibrations*

As discussed in §1.1, our experiment measures the Nusselt number as a function of the three control parameters Ra, Pr, Γ and time, so there are four measurement and control systems:

(*a*) The heat flux Q injected into the top plate sets ΔT and Ra.
(*b*) The temperature at the bottom plate of the cell $T_\circ$ sets Pr.
(*c*) The temperature difference across the fluid layer ΔT and Q yield N.
(*d*) The height of the cell d gives Γ.

A multimeter measures Q, which is generated by resistive heating at the top plate of the convection cell. Five-lead AC bridge techniques measure temperatures using germanium resistive thermometry (Behringer & Ahlers 1982). Similar bridge techniques with three leads measure the cell height d using variable capacitors (Gao *et al.* 1987); d is also obtained from the conductance of the fluid layer. The balancing arm of the bridge is an inductive ratio transformer; a lockin amplifier serves as the null meter. Figure 3 shows thermometer and heater locations.

The heat flux Q is provided by two 5 kΩ non-inductively wound wire resistors (H_{Q1} and H_{Q2} in figure 3) connected in parallel and varnished to the upper plate of the convection cell. A four-lead method allows the simultaneous measurement of both the DC current and the voltage across the top plate heater.

To maintain the temperature at the bottom plate of the cell and throughout the sample volume, we use an AC resistance bridge with a germanium thermometer (T_r) paired with a 10 kΩ standard resistor (S_{r10}). The output from this bridge is fed back through a temperature controller that supplies a voltage to one of several heaters. The heater most frequently used is a 5 kΩ resistor (H_1) on the isothermal platform. In addition there are two 5 kΩ heaters directly on the sample chamber, but heating at the isothermal platform gave better stability and less noise. The thermometer bridge ratio was calibrated against both the ^{3}He T_{62} and ^{4}He T_{58} vapour pressure temperature scales. The vapour pressure was measured using a Texas Instruments Bourdon capsule pressure gauge, which in turn was calibrated against mercury and oil manometers.

To measure ΔT, we use a differential AC bridge with germanium thermometers embedded in the top plate and in the bottom plate of the convection cell. The top plate thermometer T_t fits in a hole drilled into the centre of the top copper block. The bottom plate thermometer T_b is mounted on a long copper rod screwed into the centre of the height-changing piston, making good thermal contact near the upper part of the piston, and ensuring negligible temperature gradients between the bottom of the convection space and the thermometer. The temperature resolution ΔT is about 0.3 μK with temperature differences at the onset of convection ΔT_c ranging from 0.3 to 10 mK; hence, $3 \times 10^{-5} \leqslant \Delta T/\Delta T_c \leqslant 10^{-3}$.

The measured ΔT is not due to the fluid alone. Sidewall conductance, self-heating of the top plate thermometer, changes in κ_{eff} across the layer for very large ΔT, and Kapitza (boundary) resistance all contribute to the measured temperature difference across the fluid layer. We have ignored the effect of the Kapitza resistance, which should be negligible for $T > 0.8$ K (Pollack 1969). The other corrections have been directly and precisely measured. In the worst case, corrections amount to 20% of the total ΔT across the layer and account typically for less than 10%.

To measure the layer height, we use two independent techniques. In the first, we use an AC differential bridge with two variable capacitors. The capacitor plates are polished copper disks 1 cm in diameter that are epoxied into a copper holder. The

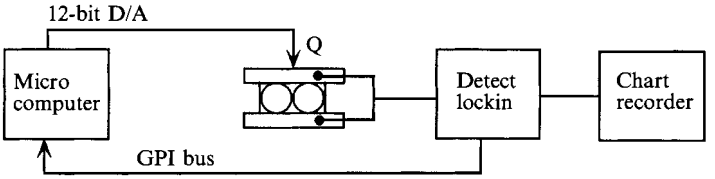

FIGURE 4. Block diagram for computer-controlled data acquisition. An AT-PC controls the heat flux with a 12-bit digital-to-analogue board and monitors several instruments on a GPI bus. A multimeter reports the heat flux at the top of the cell. The lockin amplifier reports the resulting ΔT. Lockin output is also displayed on a chart recorder.

bottom plate of the top capacitor C_t and the top plate of the bottom capacitor C_b are fixed in position on the sample chamber. The top plate of C_t moves with the cell stage, and the bottom plate of C_b moves with the bottom stage. When d is decreased, the distance between the plates of C_b decreases, while that between the plates of C_t increases by the same amount. The capacitance bridge ratio is calibrated against d at room temperature using a cathetometer and a machinist's levelling gauge. The fully closed position provides a convenient reference point. There is less than a 4% constant shift in the calibration after cooling to low temperatures. The bridge measurements of the cell height are accurate to about 5 parts in 10^4, or a little better then 10 μm. We have a comparable measurement of the length l_x of the cell. Taking into account the accuracy of both l_x and d, we know Γ to better than 1% for d above 0.5 mm and to 2.5% for d as small as 0.2 mm, which is the shortest height used in this work. The longest time spent at any single height was 4 months at $d = 0.2855$ cm. Over this time the capacitance bridge ratio shifted by less than 10 p.p.m., implying a similar stability in d.

Another way to measure the cell height is to measure the thermal conductance C_h of the layer. More specifically, very precise ratios of heights are obtained from ratios of conductances at fixed temperature. If the effective conductivity is κ_{eff} and ΔT is the temperature difference across the layer in response to a heat flux Q, then the resistance is defined as

$$\Omega = \Delta T/Q = d/\kappa_{eff}. \tag{2.1}$$

Because it is proportional to d, Ω provides a convenient way to check the capacitative calibration *in situ*. Ω also contains a Kapitza resistance component, which is independent of the height. In practice, this term is only important when d is small, in which event we use the capacitive technique to determine the height. At a fixed temperature the ratio of any two cell heights is

$$d_1/d_2 = \Omega_1/\Omega_2; \tag{2.2}$$

d itself is obtained from this procedure by using a seed height from the calibration.

2.6. *Automated data acquisition*

Data acquisition for these experiments is fully controlled by a computer, which can take data unattended for days at a time. The computer uses a 12 bit digital-to-analogue board to supply and control voltage to the top plate heater and also supervises a lockin amplifier, programmable ratio transformer, and multimeter through a GPI bus. The programmability allows more versatile and sophisticated data-taking automation than was feasible in previous experiments (Gao *et al.* 1987). Figure 4 shows a block diagram of the computer-controlled data-taking system.

To take data we first fix T_0 and d. Then the heat flux Q applied to the top plate of the cell is raised to some convenient starting value and control turned over to the computer. The data taken are either in the form of time series at a fixed heat flux or Nusselt curves (N *vs.* ΔT) for incrementally increasing heat flux.

For Nusselt curves we apply a steady Q to the top plate of the cell, and, after allowing a sufficient relaxation time, the resulting ΔT is measured by taking a 100-point time series with $\Delta t = 1$ s. These 100 values are averaged to produce ΔT for the point. Q is then raised a pre-set amount, and the procedure repeated to acquire another point. The fluid thermal relaxation time depends on both the mean temperature and the height of the layer. Usually waiting 5–10 vertical thermal diffusion times is more than sufficient to ensure the data point represents a fully relaxed fluid layer. But to guarantee relaxation, the control software waits a pre-set amount of time and then takes a trial 100-point time series. The software fits a straight line to these trial points, and, if the slope of the line is close enough to zero, it accepts the average of the trial points. If the slope is too big, new trial points are acquired – over and over again until the fluid is fully relaxed.

3. Theory and measurements for the onset of convection

The equations of motion for SMC resemble the Boussinesq equations for RBC but with additional terms from superfluid effects. To the extent that the superfluid effects are small, SMC should behave like standard RBC. The onset of convection is currently the only point at which to rigorously measure superfluid deviations from classical RBC behaviour because there is no analysis of the nonlinear states of SMC above onset. It is only through the linear stability problem for the critical Rayleigh number and critical wavevector that we can combine analysis and experiment to interpret and quantify superfluid effects.

Parshin (1969) made an early analysis of the linear stability problem by assuming that c and T were completely coupled. More specifically, he assumed that μ_4 and P were constant and that $\nabla \cdot \boldsymbol{v}_n = 0$. This is the zeroth-order approach to this problem and leads to a critical Rayleigh number that is the same as that classically calculated ($Ra_c \approx 1708$), but with several hydrodynamic quantities, such as the thermal diffusivity, redefined to reflect superfluid qualities. Steinberg (1981*a*, *b*) and Fetter (1982*a*, *b*) have formulated the SMC onset problem allowing deviations in μ_4 and $\nabla \cdot \boldsymbol{v}_n$. Steinberg (1981*a*, *b*) casts the SMC linearized equations of motion in variables of velocity and entropy with free–free boundary conditions, and solves for Ra_c in two limiting cases. Fetter (1982*a*, *b*) casts the SMC linearized equations of motion in variables of velocity, temperature and pressure with rigid boundary conditions, and solves for Ra_c approximately by treating the superfluid terms as perturbations. Metcalfe & Behringer (1993) have extended the analysis to facilitate direct experimental comparison and also to calculate the SMC critical wavevector. There is no *a priori* justification for considering superfluid terms to be small: the circumstances of the validity of this assumption must be determined by experiment. In this section we first discuss the linear stability analysis of SMC, then present the measurements of the superfluid effects, and finally make comparisons to theory.

3.1. *Linear stability analysis*

The SMC equations of motion are approximations of Khalatnikov's (1965) hydrodynamic equations of motion for ^{3}He-superfluid-^{4}He mixtures, just as the Boussi-

nesq equations are approximations of the Navier–Stokes equations. After non-dimensionalizing and linearizing the equations of motion about the pre-convective steady state, we arrive at the following set of equations describing the stability of a laterally infinite layer of dilute superfluid mixture subjected to a destabilizing temperature gradient (Fetter 1982*a*, *b*):

$$\nabla^2 \boldsymbol{v}_n - T\hat{\boldsymbol{z}} - \nabla P + \epsilon_1 \frac{\partial \boldsymbol{v}_n}{\partial z} + \left[\epsilon_1 \frac{\rho}{\rho_s} - \epsilon_3\right] \epsilon_2 v_{nz} \hat{\boldsymbol{z}} = 0, \tag{3.1a}$$

$$Ra^{-1} \nabla^2 T - v_{nz} = 0, \tag{3.1b}$$

$$\nabla \cdot \boldsymbol{v}_n - \epsilon_2 v_{nz} = 0. \tag{3.1c}$$

As in the classical problem, v_n, T, and P are perturbations on the pre-convective steady-state solutions of (normal fluid) velocity, temperature and pressure, and we seek to know whether eigenfunctions of (3.1) will grow or decay.

The ϵ_i quantify the superfluid effects. Except for the terms involving the ϵ_i, (3.1) are the linearized equations for the onset of RBC. (Compare for example equations 55–57 of Chandrasekhar 1961.) The ϵ_i are defined by

$$\epsilon_1 = -v_{nz}^{\circ}, \tag{3.2a}$$

$$\epsilon_2 = \gamma \Delta T / T^{\circ}, \tag{3.2b}$$

$$\epsilon_3 = \frac{\rho g d \beta_c}{\left|\left(\partial \mu_4 / \partial c\right)_{T,P}\right|} \frac{\zeta_1 - \rho \zeta_3}{\eta}. \tag{3.2c}$$

Variables superscripted with $\circ$'s are the linear, steady solutions, and

$$\gamma = (T/c)(\partial c / \partial T)_{P,\mu_4}. \tag{3.3}$$

Each ϵ_i represents a distinct physical effect (Fetter 1982*a*, *b*): ϵ_1 counterflow advection (the $\epsilon_1 \partial_z$ term) augments heat conduction; ϵ_2 volume changes equivalent to compressibility effects are allowed in $\boldsymbol{v}_n$ (3.1*c*) even though $\nabla \cdot \boldsymbol{j} = 0$ (§1.4); ϵ_3 superfluid dissipation processes ($\zeta_{1,3}$ are second viscosity coefficients) that have no comparable analogue in RBC. As there are no direct measurements of $\zeta_1 - \rho\zeta_3$, ϵ_3 is poorly known. Unfortunately, the product $\epsilon_2 \epsilon_3$ is the crucial quantity determining the size of superfluid effects. This is why we must measure the size of superfluid corrections.

Assuming the ϵ_i to be small parameters, Fetter (1982*a*, *b*) has carried out a perturbation solution of (3.1) to find Ra_c. However, a solution in terms of the ϵ_i does not offer much guidance as to how to measure superfluid effects in an experiment. Metcalfe & Behringer (1993) have reformulated and extended the perturbation analysis to use the inverse layer height d^{-1} as the small parameter. They have shown that only even powers of d^{-1} are needed and have calculated Ra_c and q_c, the critical wavevector. The expansion result for Ra_c is

$$Ra_c / Ra_{c\circ} = 1 + p_3 \left(\lambda_\circ / d\right)^2 + (p_3 + p_4) R_{c\circ} \left(\lambda_\circ / d\right)^4 + O(d^{-6}), \tag{3.4}$$

where $Ra_{c\circ} = 1707.7\ldots$ is the critical Rayleigh number for RBC; p_3 and p_4 are wavevector-dependent functions with $p_3 \lesssim 20$ and $p_4 \sim 10^{-4}$ for $q = 3.114$; and $\lambda_\circ$ is

a characteristic length scale defined as

$$\lambda_\circ^2 = \frac{\beta_c \chi_{eff} (\zeta_1 - \rho\zeta_3) (\partial c/\partial T)_{P,\mu_4}}{c \left| \alpha_{P,\mu_4} (\partial \mu_4/\partial c)_{T,P} \right|}. \tag{3.5}$$

Superfluid effects shift $Ra_c > Ra_{co}$, but these effects will be small when $d \gg \lambda_\circ$. This analysis makes it transparent that superfluid effects can be directly measured through the change in Ra_c as d is varied.

However, (3.4) is a divergent series. The $O(d^{-2n})$ coefficient grows as Ra_{co}^{n-1}. For this reason the truncated series expansion does not accurately predict Ra_c for $\lambda_\circ/d \gtrsim 5\times10^{-2}$. Equation (3.4) does, though, correctly predict the dominant superfluid effect, which is embodied in the term $\epsilon_2\epsilon_3 = Ra_{co}(\lambda_\circ/d)^2$. The deficiencies of the series solution may be remedied and also more insight into the physics afforded by analysis of a simplified version of (3.1) that contains only the leading-order superfluid effect.

First combine (3.1) into a single equation for v_{nz}, namely

$$\begin{aligned}(\partial^2 - q^2)^3 v_{nz} - q^2\tilde{c}(\partial^2 - q^2)v_{nz} - (\epsilon_1\epsilon_2)(\partial^2 - q^2)\partial^2 v_{nz} \\ +(\epsilon_2 - \epsilon_1)(\partial^2 - q^2)\left[q^2\partial - \partial^3\right] v_{nz} = -q^2 Ra v_{nz},\end{aligned} \tag{3.6}$$

where $\tilde{c} \equiv \left[\epsilon_1(\rho/\rho_s) - \epsilon_3\right]\epsilon_2$ contains the leading superfluid term $\epsilon_2\epsilon_3$. The first terms on the left- and the right-hand sides of (3.6) are classical (Chandrasekhar 1961), equation 198. The second term of the left-hand side is even in z, while the fourth term is odd. Since v_{nz} must be even to obtain the lowest value of Ra_c, we drop the odd term. In any event, terms involving ϵ_1 and ϵ_2 alone, without ϵ_3, are small for the current experimental conditions. Also, we neglect counterflow advection by setting $\epsilon_1 = 0$. A careful analysis (Metcalfe & Behringer 1993) shows that each of these approximations are accurate to at least 1% for the concentrations and temperatures of the present experiments. These two simplifications have the effect of removing all non-Hermitian terms from (3.1), leaving the approximate equation

$$(\partial^2 - q^2)^3 v_{nz} + q^2\epsilon_2\epsilon_3(\partial^2 - q^2)v_{nz} = -q^2 R v_{nz} \tag{3.7}$$

which is exactly solvable. The boundary conditions for (3.7) are

$$v_{nz} = \partial v_{nz} = (\partial^2 - q^2)^2 v_{nz} = 0 \tag{3.8}$$

for $z = \pm 1/2$, which are appropriate for rigid boundaries.

Substituting the ansatz $v_{nz} = A_\circ \cos(b_\circ z) + A\cosh(bz) + A^* \cosh(b^* z)$ into (3.7) leads to the transcendental equation

$$\frac{(b_2\sqrt{3} + b_1 D)\sinh(b_1) + (b_1\sqrt{3} - b_2 D)\sinh(b_2)}{\cosh(b_1) + \cos(b_2)} = -D b_\circ \tan(b_\circ/2), \tag{3.9}$$

as the compatibility condition for the solution of (3.7). The quantities $\pm i b_\circ$, $\pm(b_1 \pm i b_2)$ are the roots of the characteristic equation

$$(b^2 - q^2)^3 + q^2\epsilon_2\epsilon_3(b^2 - q^2) + q^2 R = 0. \tag{3.10}$$

Solutions of (3.9) implicitly relate (for a given $\epsilon_2\epsilon_3$) Ra and q and map out the marginal stability curve $Ra(q)$. In the limit $\epsilon_2\epsilon_3 \to 0$, (3.9) recovers the RBC result (Chandrasekhar 1961, equation 216, chap. II). Figure 5 shows Ra_c and q_c as a function of $(\lambda_\circ/d)$ from the simplified model (3.9) and from the first two terms of the expansion (3.4). This figure demonstrates that the effects of the superfluid corrections on both R_c and q_c are minimal for $\lambda_\circ/d < 0.1$. In the limit that $\epsilon_2\epsilon_3$ becomes large (large $\lambda_\circ/d$),

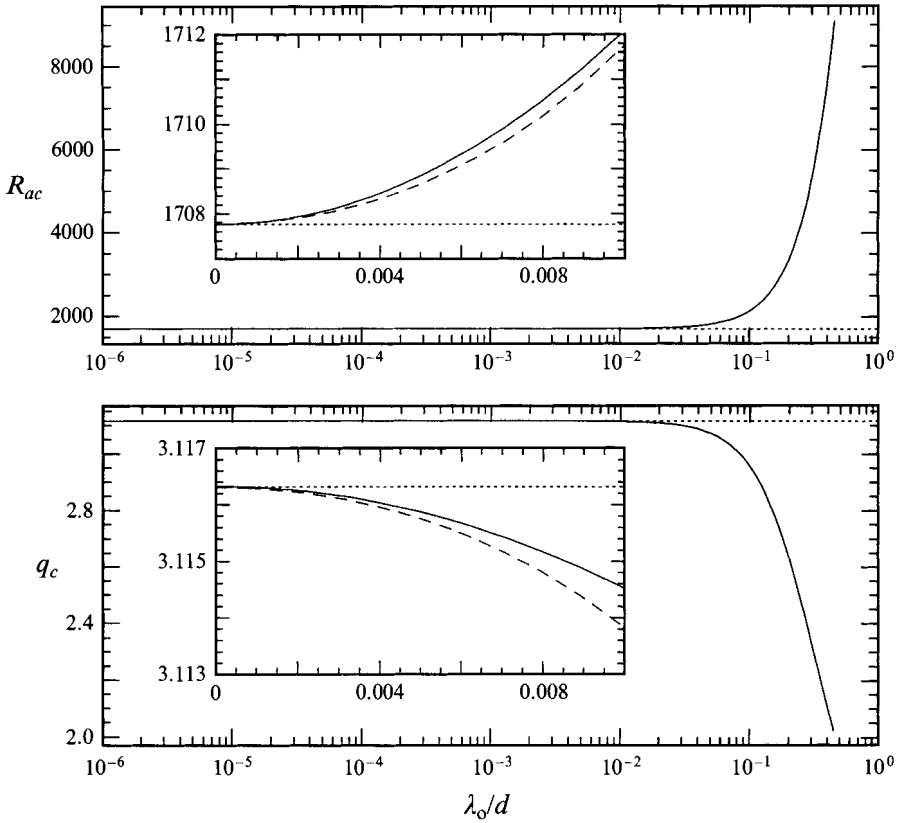

FIGURE 5. Ra_c and q_c from the simplified model (solid line) and from the first two terms of the expansion (dashed line) as functions of λ_o/d. Ra_c and q_c are on linear scales; λ_o/d is on a $\log_{10}$ scale. The insets both have linear–linear scales. For λ_o/d large enough the only solution is $q = 0$. The dotted lines mark Ra_{co} and q_{co}.

the only solution of (3.9) is $q = 0$: Ra_c is elevated and q_c depressed. The dominant superfluid effect increases the roll wavelength, inhibiting convection. The result for q_c, in particular, is important for large aspect ratios, which are typically achieved by making d small. We note that previous theoretical work only considered the effect of the superfluid terms on Ra_c.

Until they are very large, superfluid effects only shift the values of Ra_c and q_c from their classical values. Other features of RBC are unaffected, for instance the shape of the marginal stability curve. Figure 6 shows as solid lines the marginal stability curves for $\lambda_o/d = 0$ and 10^{-2}; the dashed line shows the $\lambda_o/d = 10^{-2}$ curve with the constant shift in Ra_c subtracted out, while the dotted line shows the same curve with both the constant Ra_c and q_c shifts subtracted. The dotted line is hard to see as it overlays the classical curve except at extreme values of q. In particular, figure 6 shows that the curvature of $Ra(q)$ in the vicinity of Ra_c is unaltered by superfluid effects. In the highly successful amplitude formalism describing (weakly) nonlinear convection, one of the chief parameters is the correlation length, which is the curvature of $Ra(q)$ at Ra_c Cross (*1980*). While the amplitude equations describing SMC are currently underived, they should be similar to those describing RBC.

The above analysis shows that, to a good approximation, all superfluid effects are

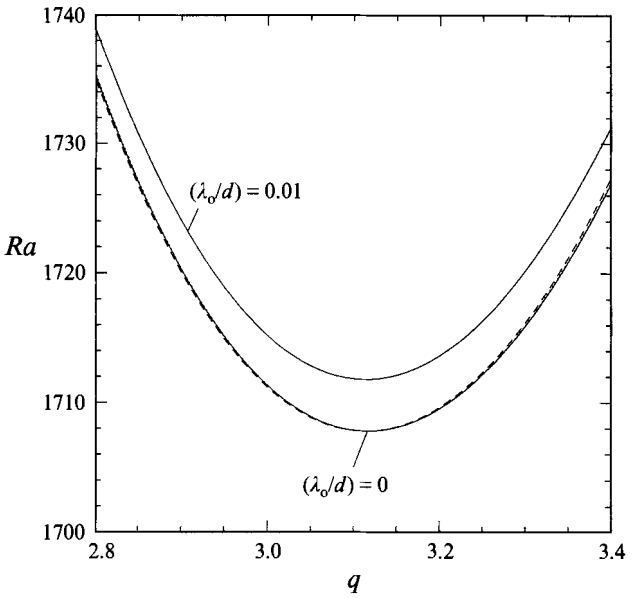

FIGURE 6. $Ra(q)$ for the indicated values of $\lambda_\circ/d$. The dashed line is the data for $\lambda_\circ/d = 0.01$ with the shift in Ra_c subtracted out. The dotted line, which almost perfectly overlays the $\lambda_\circ/d = 0$ curve, is the dashed line with the shifts in Ra_c and q_c subtracted.

contained in the length scale $\lambda_\circ$, which can be measured through its effect on the critical Rayleigh number Ra_c as the cell height is varied.

3.2. *Measurement of the superfluid effects*

The raw data of these experiments are converted to Nusselt curves, the function $N(Ra)$. Figure 7 shows representative Nusselt data for a range of temperatures and for aspect ratios $\Gamma \approx 14$. At Ra_c, N should change from $N = 1$ to

$$N = 1 + S\epsilon + \cdots, \tag{3.11}$$

where

$$\epsilon \equiv (Ra - Ra_c)/Ra_c. \tag{3.12}$$

The point at which N rises above unity determines ΔT_c which is crucial to our analysis for the superfluid corrections. The sharpness of the change in $\mathrm{d}N/\mathrm{d}(Ra)$ at Ra_c usually provides insight into geometric imperfections, i.e. a rounded transition may signify non-uniformities in d. The parameter S provides information on the convective amplitude. Well above onset $N(Ra)$ provides a signature for changes of the convective pattern or state.

In determining N we use the corrected (cf. the discussion in §2.5) heat flux Q and ΔT to determine the overall effective thermal conductivity, which depends only on the fluid properties and the state of the fluid (i.e. convecting or not). We then normalize this result by the value for the effective conductivity well below the onset of convection.

The data for $N(Ra)$ follow horizontal straight lines below Ra_c. After onset there is a short region in Ra with a slight linear rise, followed sharply by another linear rise with much greater slope where convection has clearly set in. In order to empirically capture this feature and obtain as unbiased a determination of ΔT_c as possible, we

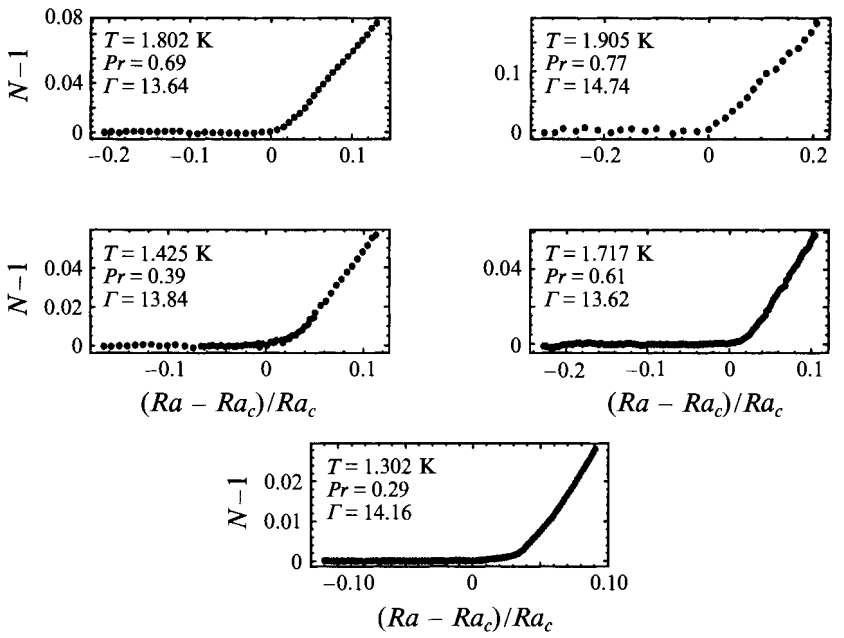

FIGURE 7. Data for $N-1$ versus $\epsilon = (Ra-Ra_c)/Ra_c$ for five temperatures spanning the temperature range covered by the present experiments. These data were obtained for essentially the same height ($d = 0.1633$ cm, within 0.0083 cm).

first select points clearly below onset and fit them to a straight line to account for the weak temperature-dependence of the thermal conductance. The shape of the data immediately above onset suggests an appropriate fitting function is one that interpolates between two straight lines, for instance

$$N(\Delta T) = a_1 + a_2(\Delta T - a_4) + a_3(\Delta T - a_4)\tanh[(\Delta T - a_4)/a_5]. \tag{3.13}$$

For small ΔT (3.13) is a straight line. For large ΔT (3.13) is again a straight line; a_5 gives the width of the crossover region between the two lines. The other parameters combine to give the slopes and intercepts of the straight line segments. With five adjustable parameters, the fit is always good. Similar functions were tried but did no better job of fitting the data. Obtaining ΔT_c in the presence of a rounded transition is frequently encountered and slightly different strategies are in use. Ahlers (1974), Haucke *et al.* (1981) and Gao *et al.* (1987) fit straight lines to the data well above and well below the rounded region with the intersection of the lines determining ΔT_c. This involves a four-parameter fit plus two other parameters which estimate the boundaries of the rounded region. We also fit the data in this manner. ΔT_c determined by the two methods may differ by at most a few percent. Finding the zero of the function $N(\Delta T) - 1$ experimentally defines the critical temperature difference ΔT_c.

Figure 8 shows the results of extensive measurements of $Ra_c(d)/Ra_{c\infty}$ versus d^{-2} for a number of temperatures. $Ra_c(d)/Ra_{c\infty}$ is derived from ΔT_c in the following way. At each mean temperature, we make a linear fit of $d^3\Delta T_c$ to d^{-2} as suggested by (3.4):

$$d^3\Delta T_c = A + Bd^{-2}, \tag{3.14}$$

where A and B are the fit coefficients. The data for small d^{-2} at $T = 1.050$ correspond to very low aspect ratios where the effect of the sidewalls elevates the critical Rayleigh

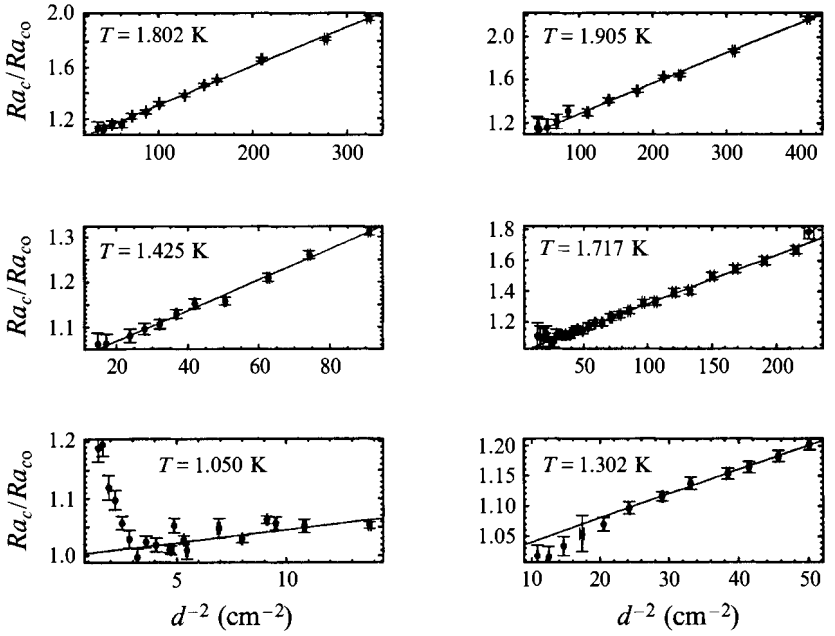

FIGURE 8. Data for Ra_c/Ra_{co} versus d^{-2}, the inverse square of the layer height. The mean temperature of each data set is indicated.

number; we do not include these data in the fits. $Ra_c(d)/Ra_{co}$ is operationally obtained from (3.14) through normalization by A. This is more accurate than constructing Ra_c directly because none of the fluid parameters comprising Ra_c are as well measured as d and ΔT_c. With this normalization uncertainties from the fluid parameters are removed. The solid lines in figure 8 are fits of (3.14) to the data; error bars show the statistical uncertainties. The quality of the fits in figure 8 is good. Use of the quartic terms does not significantly improve the fits, and λ_o is obtained as

$$\lambda_o^2 = (B/A)p_3^{-1} \tag{3.15}$$

by comparing (3.14) with the first term of (3.4). The superfluid characteristic length scale λ_o is shown versus temperature in figure 9.

That higher-order terms are not needed to fit the data may seem somewhat surprising. The experimental values of λ_o/d range from 0.02 to 0.3, and for $\lambda_o/d = 0.1$ the ratio of the $O(d^{-4})$ term to the $O(d^{-2})$ term is 17. The fourth-order term should make a significant contribution. That this is not the case is another indication that the series solution (3.4) cannot be used for quantitative comparisons, except for very small λ_o/d.

It is noteworthy that λ_o drops with increasing temperature. This implies that SMC more closely approximates RBC for fixed d as T_o increases. However, this does not imply that we can reduce superfluid effects at onset to arbitrarily small levels by operating at higher temperatures. Experimentally, ΔT_c (shown versus temperature for a fixed height in figure 10) decreases very rapidly with increasing temperature. Thus, while the intrinsic size of superfluid effects at onset may be shrinking, experimentally, they become more important because d must be decreased to boost ΔT_c to a resolvable level. Ever smaller superfluid terms, though, could be obtained by using thermometry with ever better resolution (Ahlers & Duncan 1988; Lipa & Chui 1987).

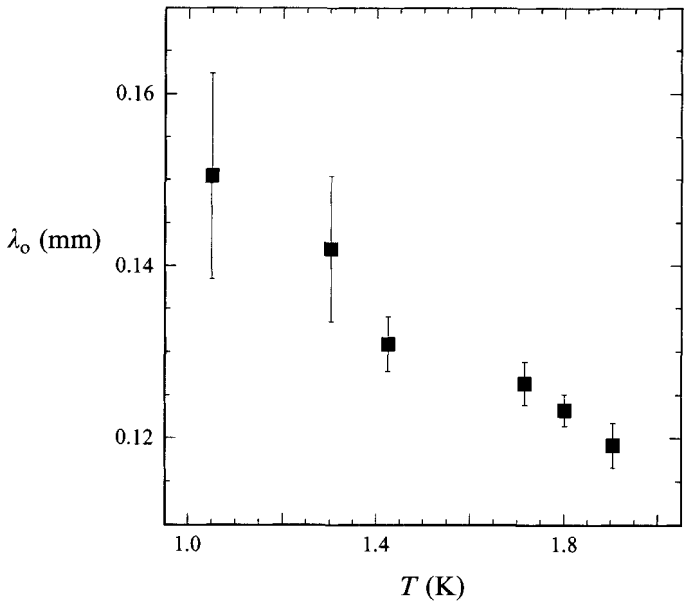

FIGURE 9. The superfluid characteristic length scale λ_0 versus temperature.

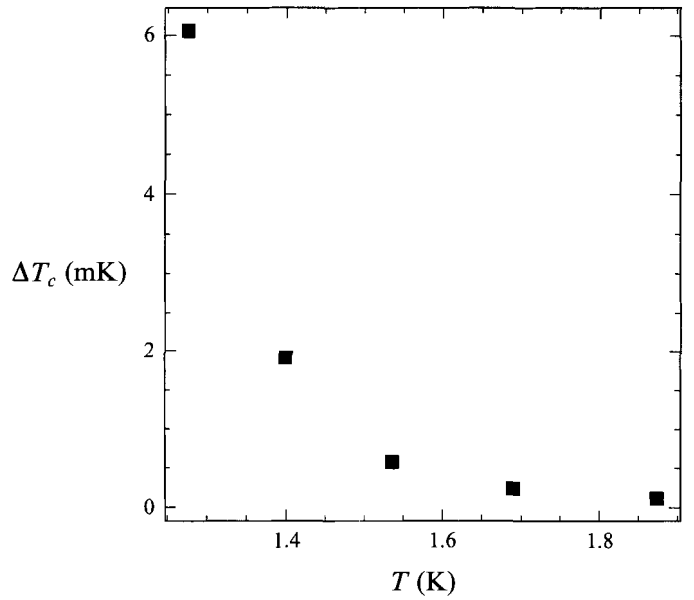

FIGURE 10. Values of the critical temperature difference for the single height $d = 0.1633$ cm.

3.3. *Comparison of theory and experiment*

Both the simplified model and the expansion (in the range of helium parameters considered here) predict that there is only one relevant parameter, the length scale λ_0, associated with superfluid deviations of SMC from RBC. Thus, at each mean temperature, scaling d by λ_0 should collapse all the measurements of $Ra_c(d)/Ra_{c0}$ onto a single curve. We test this idea in figure 11. The data are the solid symbols; the solid line shows the expansion result to $O(d^{-2})$; the dashed line shows the expansion

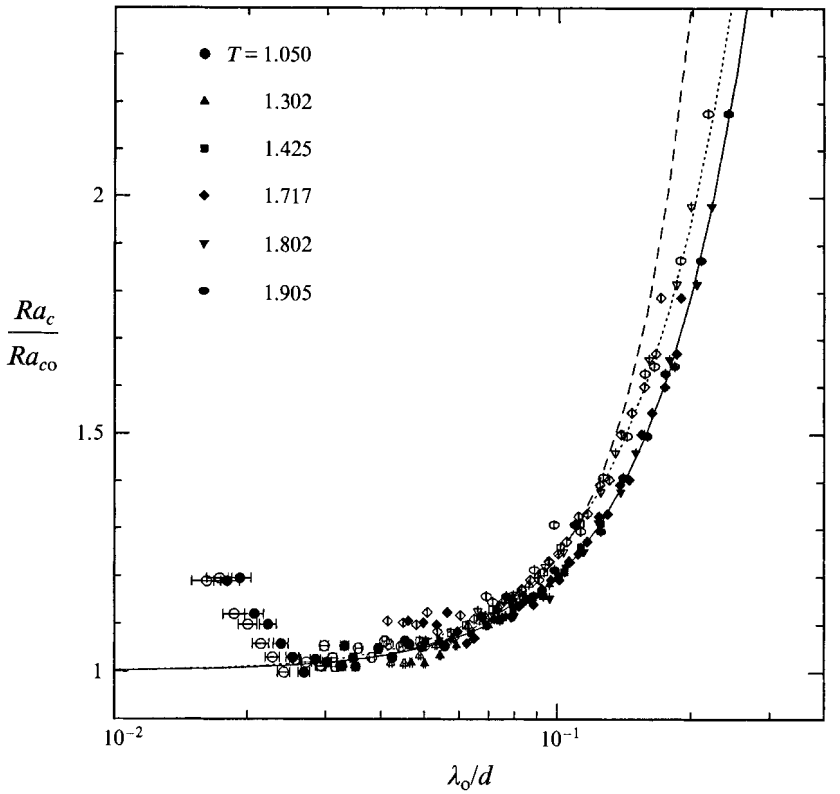

FIGURE 11. Ra_c versus λ_o/d on log–linear scales comparing theory and experimental. When d is scaled by λ_o the data (solid points) fall onto a universal curve independent of the temperature, which is indicated for each data set. The dotted line shows the exact solution of the simplified model; the solid line shows the first term of the expansion; and the dashed line shows the first two terms of the expansion. Open symbols are the data with λ_o uniformly reduced by 10%.

result to $O(d^{-4})$; and the dotted line shows the exact solution of the simplified model. We also plot the data using values of λ_o uniformly decreased by less than 10% (open symbols). This shift, which is within the error bars for λ_o, brings the simplified model into essentially perfect agreement with the data except at the lowest values of λ_o/d where Ra_c is elevated by small aspect ratio effects.

3.4. *Some comments on the physical interpretation of* λ_o

We conclude this section with some comments on the physical interpretation of λ_o. Before the onset of convection, the deviations of the steady-state concentration and temperature from the equilibrium values c_o and T_o are linear functions of z which are linked by

$$c - c_o = \frac{-\gamma c}{T}(T - T_o). \tag{3.16}$$

The resulting buoyancy force per unit volume is

$$\boldsymbol{F}_b = \rho g \hat{\boldsymbol{z}}[\alpha_{P,c}(T - T_o) + \beta_c(c - c_o)], \tag{3.17}$$

which when combined with (3.16) yields a force $\boldsymbol{F}_b = \rho g \hat{\boldsymbol{z}} \alpha_{P,\mu_4}(T - T_\circ)$ with an effective expansion coefficient $\alpha_{P,\mu_4} = \alpha_{P,c} - (\gamma c/T)\beta_c$. Since $\alpha_{P,\mu_4} < 0$†, $\boldsymbol{F}_b$ is directed in the $-\hat{\boldsymbol{z}}$-direction when T exceeds the reference temperature.

When convection begins, neglecting squared velocity terms, (3.16) acquires a new term to become

$$c - c_\circ = \frac{-\gamma c}{T}(T - T_\circ) + \frac{\zeta_1 - \rho\zeta_3}{(\partial\mu_4/\partial c)_{P,T}} \nabla \cdot \boldsymbol{v}_n. \tag{3.18}$$

The resulting new term in the buoyancy force is

$$\boldsymbol{F}_d = \rho g \hat{\boldsymbol{z}} \left[\beta_c \frac{\zeta_1 - \rho\zeta_3}{(\partial\mu_4/\partial c)_{P,T}} \nabla \cdot \boldsymbol{v}_n \right]. \tag{3.19}$$

Non-dimensionalizing and putting $\boldsymbol{F}_d$ in terms of the ϵ_i gives the drag force

$$\boldsymbol{F}_d = \hat{\boldsymbol{z}} \epsilon_2 \epsilon_3 v_{nz}. \tag{3.20}$$

We refer to $\boldsymbol{F}_d$ as a drag force because, owing to superfluid dissipation, this leading-order superfluid effect reduces the buoyancy over a length $\lambda_\circ$. The width of a roll is (at $q_{c\circ}$) approximately d, and the length $\lambda_\circ$ could indicate the range of superfluid interaction between up- and down-welling flows. The most important thing to notice is that whenever the cell height $d \gg \lambda_\circ$, the superfluid effects will be negligible. This implies that there is a broad range of operating temperatures for which SMC, at least at onset, is a close analogue to RBC.

4. Secondary instabilities

When $\lambda_\circ/d$ is small, it is likely that the nonlinear states of SMC also closely approximate the nonlinear states of RBC. However, because there are no calculations of the nonlinear effects of the superfluid terms in (3.1), this assumption cannot be rigorously tested, as it has been near onset. Corroborating evidence is possible, though, through comparison of the measured location and type of SMC nonlinear roll instabilities to predictions from RBC calculations.

Extensive calculations of the instabilities of straight parallel convection rolls have been carried out by Busse & Clever (Clever & Busse 1974; Busse & Clever 1979; Bolton, Busse & Clever 1986). For a horizontally infinite layer of fluid and for various Ra and Pr, these authors compute steady solutions of straight parallel rolls at a given wavevector and then examine the linear stability of the roll solutions. Various types of destabilizing modes and their location in Ra–Pr–q space have been identified in this way. Figure 12 shows several slices at constant values of Pr from this space showing the stability boundaries for the oscillatory instability and skewed-varicose instability, which are the relevant instabilities for $Pr < 1$. At the oscillatory instability, a wavy disturbance undulates perpendicularly to the roll wavevector with a single frequency. We note several experimental studies of the oscillatory instability Libchaber, Fauve & Laroche (1983), Chiffaudel, Perrin & Fuave (1989), and in particular recent experiments by Ecke and coworkers (Ecke *et al.* 1986; Deissler, Ecke & Haucke 1987; Mainieri, Sullivan & Ecke 1989) using superfluid mixtures in a small aspect ratio container. At the skewed-varicose instability a bending disturbance initiates roll distortion, and in experiments leads to roll annihilation

† An extensive tabulation of fluid parameters for dilute superfluid mixtures is available on request from the authors or the JFM Editorial Office.

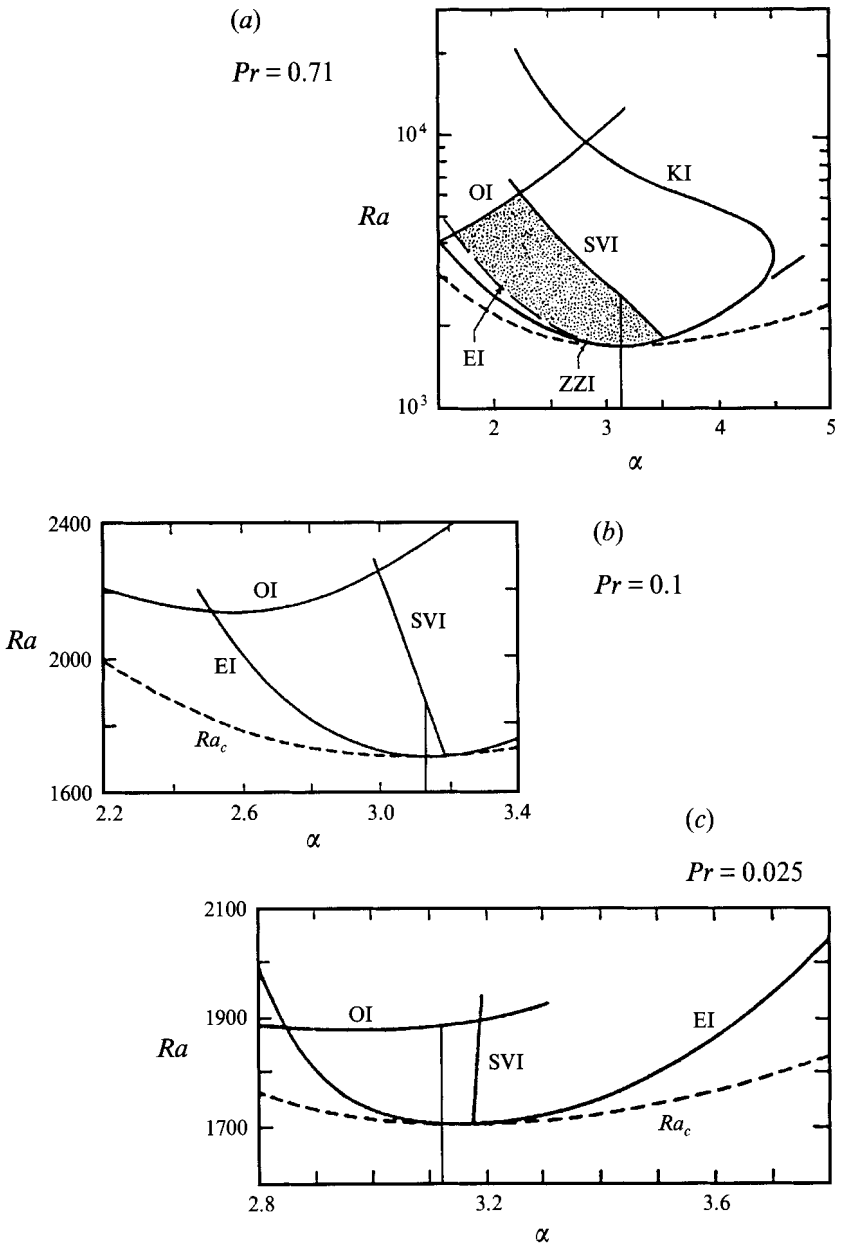

FIGURE 12. Constant Prandtl number cuts, after Clever & Busse (1974), Clever & Busse (1978) and Busse & Clever (1979), from the Busse balloon showing instability boundaries as functions of Rayleigh number and wavevector. Prandtl numbers for each cut are indicated. Inside the lines straight rolls are stable, as indicated by the shaded region in (*a*). The labelled instabilities are Eckhaus (EI), zig-zag (ZZI), knot (KI), skewed-varicose (SVI), and oscillatory (OI). The thin line extending up from the α-axis shows the path for $\alpha = \alpha_c$. In our notation $\alpha = q$. The dashed lines in each figure show the Pr-independent linear instability of the conducting state.

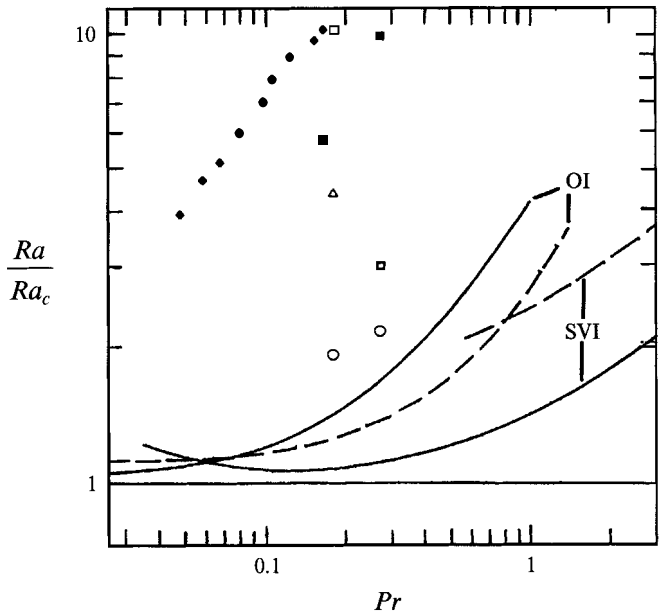

FIGURE 13. Lines show the stability boundaries for the oscillatory and skewed-varicose instabilities as computed by Clever & Busse (1974, 1978, 1979) for wavevectors $q = 3.117$ (solid) and $q = 2.2$ (dashed). Symbols show data for comparison. Open symbols indicate transitions from steady to steady convection; solid symbols indicate transitions from steady to time-dependent convection: ○, $\Gamma = 8.0$; □, 4.0; △, 6.0. ◇; data of Maeno *et al.* (1985) taken in a $\Gamma = 1$ cylindrical cell.

and the reduction of the wavevector back into the stable band; however, roll annihilation is a nonlinear process not accessible to the stability calculations and is not entirely understood (Newell *et al.* 1990). There have been several studies of the skewed-varicose instability using argon gas and (non-superfluid) liquid ^{4}He (Croquette 1989*a*, *b*; Motsay, Anderson & Behringer 1988). There is no previous work on the skewed-varicose instability in SMC.

The skewed-varicose instability and oscillatory instability boundaries in figure 12 nominally cross at a codimension-2 point that depends on the Prandtl number and the wavevector of the initial roll pattern. In the neighborhood of this point there is a large variety of unexpected behaviour that we will examine in Part 2. The calculations in figure 13 show the instability boundaries as a function of Pr for $q = 3.117$ (solid line) and $q = 2.2$ (dashed line). The symbols show the data discussed below. The predicted Pr for the crossing point for $q = q_{co} = 3.117$ is $Pr \approx 0.06$, but for $q = 2.2$ the predicted crossing point moves an order of magnitude to $Pr \approx 0.8$, i.e. the predicted location of the codimension-2 point is very sensitive to wavevector shifts. Because superfluid effects tend to reduce q_c, we might expect the codimension-2 point to occur at a higher Pr for a superfluid mixture than for a conventional fluid. However, even for a Boussinesq fluid, we could not expect perfect agreement between an experiment and predictions for the codimension-2 location, owing to the finite aspect ratio of an experimental convection cell. Nonetheless, if the location of the codimension-2 point in SMC experiments is close to that predicted by RBC calculations, which is the case

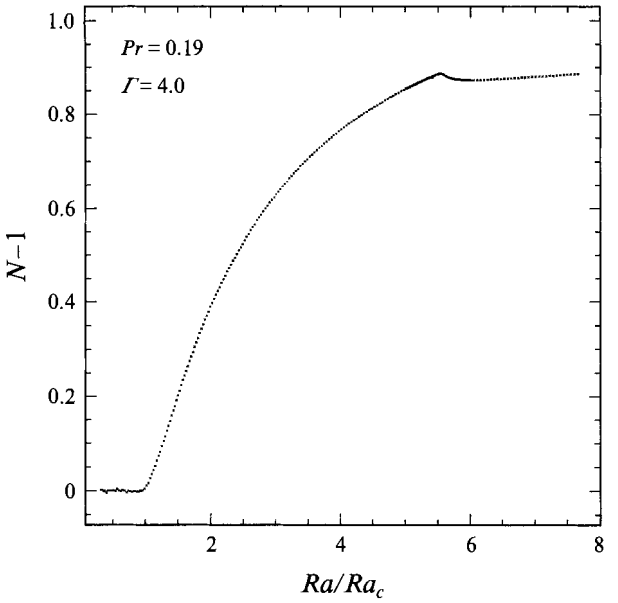

FIGURE 14. Nusselt curve of Pr slightly below that for the crossing of the skewed-varicose and oscillatory instabilities. Here, the first roll instability is the oscillatory instability. At $Ra/Ra_c = 5.6$ there is a Hopf bifurcation with a frequency in good agreement with predictions for a roll planform at $Pr = 0.19$ and $q = q_c$. Note the cusp in N as oscillations begin.

in these experiments, that is an indication that the SMC–RBC analogy may remain valid well above onset, providing the experimental conditions are well chosen.

We find that the crossing point between the oscillatory instability and the skewed-varicose instability occurs in the range $0.19 < Pr < 0.29$. The precise wavenumbers and flow patterns are not accessible, but we expect that q will be near 3.1 when Γ is an even integer, and figures 14 and 15 show data for $\Gamma = 4.00$, 6.00, and 8.00. Note that for these aspect ratios $0.024 \leqslant \lambda_o/d \leqslant 0.049$ for a typical value of $\lambda_o = 0.14$ mm.

Figure 14 shows the Nusselt data for $Pr = 0.19$. Because low Pr is coincident with high ΔT_c, we are only able to study relatively low aspect ratios such as $\Gamma = 4.00$. In this case, there is a forward Hopf bifurcation at $Ra/Ra_c = 5.6$ with a single frequency of $f\tau_v = 8.8$, where τ_v is the vertical thermal diffusion time. The measured frequency is in good agreement with the Clever & Busse prediction that $f\tau_v = 10$ for $q = q_c = 3.114$. However, the value of Ra at onset is substantially elevated from that predicted in figure 12.

Figure 15 shows Nusselt data for $Pr = 0.29$. For $\Gamma = 4.00$ and $Pr = 0.29$, the skewed-varicose instability is the first instability of the convection rolls (leftmost arrow). There is, though, only a small decrease in N. After this transition, the system next encounters the oscillatory instability at $Ra/Ra_c = 9.3$ (rightmost arrow). Here $f\tau_v = 5.9$, while for this Pr we should expect a dimensionless frequency around 19 if the rolls were at the critical wavevector. However, if the skewed-varicose transition encountered earlier had caused the loss of a roll pair and a corresponding wavevector reduction to $q = 1.6$, then we would expect a dimensionless frequency of 6, which agrees well with the data. However, this interpretation must be treated with caution because the decrease in N at the skewed-varicose transition is small compared to what we would expect for the loss of a roll pair. For $\Gamma = 8.00$, there is a very well-defined transition seen in the Nusselt number for $Ra/Ra_c = 2.12$. Past this transition

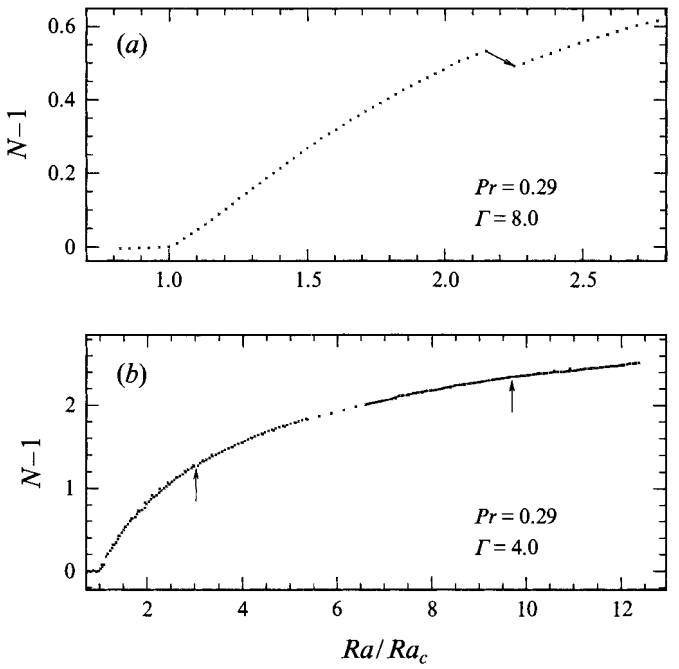

FIGURE 15. Nusselt curves for Pr slightly above that for the crossing of the skewed-varicose and oscillatory instabilities. In (*a*) there is a discontinuous transition from a state of steady convection to another steady state with lower heat transport efficiency (lower N). A lack of cooling power prevents examination of higher r at $\Gamma = 8$. The arrow in (*b*) at lower r marks a discontinuity in N, which is characteristic of the skewed-varicose instability, while the second arrow at higher r marks the oscillatory instability, which has a frequency consistent with the wavevector reduction scenario of the skewed-varicose instability.

Γ	Pr	d (cm)	T_o (K)	τ_v (s)	f (Hz)	$f\tau_v$ (obs.)	$f\tau_v$ (pred.)
4	0.19	0.5745	1.075	16.3	0.54	8.8	10
4	0.29	0.5747	1.302	32.6	0.18	5.9	19, 6†
4	0.23	0.5747	1.161	25.1	0.14	3.5	10.2
8	0.23	0.2849	1.161	6.2	0.03, 0.73	0.2, 4.5‡	10.2

† First value for $q = 3.117$; second for $q = 1.6$

‡ Several oscillatory states exist near the crossing point; see Part 2.

TABLE 1. Measured frequencies f of oscillatory states, scaled by the vertical horizontal diffusion time τ_v, as a function of Pr. For comparison the predictions of Busse & Clever (1974, 1978, 1979) for $q_c = 3.117$ (except as noted) are also shown.

point the Nusselt number drops through a long chaotic transient to a new steady state, which is entirely consistent with previous observations of the skewed-varicose instability (Kolodner *et al.* 1986; Motsay *et al.* 1988; Walden *et al.* 1987).

It is interesting to note the good agreement between the predicted and observed oscillation frequencies. Table 1 shows measured frequencies of simple oscillatory states scaled by the vertical horizontal diffusion time $\tau_v (\equiv d^2/\chi_{eff})$ as a function of Pr along with predictions of Clever & Busse (1974), Busse & Clever (1979). The

agreement between theory and experiment for $Pr = 0.19$ and 0.29 is good, and away from the crossing point agreement is to be expected since the Busse calculations have been quite successful at Prandtl numbers appropriate to mercury, (pure) helium, water and oils. In the neighborhood of the crossing, however, it is unclear how to interpret the frequencies because physical processes not accounted for in the calculations must become important. None of the frequencies at $Pr = 0.23$ can be made to reasonably fit into the Busse balloon picture.

A compilation of the data for the secondary transitions is given in figure 13. Specifically, circles show data for $\Gamma = 8.0$, triangles for $\Gamma = 6.0$ and squares for $\Gamma = 4.0$. Open symbols denote a transition from steady to steady convection, and solid symbols denote a transition from steady to oscillatory convection. For comparison, the solid diamonds show the data of Maeno *et al.* (1985) for SMC taken in a $\Gamma = 1.0$ circular cell; these data always encounter the oscillatory instability and also show good agreement with predicted frequencies. One may immediately notice from this figure that the presence of sidewalls considerably boosts the Rayleigh number for the onset of roll instabilities from that predicted for an infinite layer. Data points from the smaller aspect ratios are up to 10 times the predicted values. However, for a given Pr the larger one makes Γ, the closer one comes to the infinite layer predictions. For $\Gamma = 8.0$ the data and predictions are in disagreement by only a factor of 2. This is always the case for a small aspect ratio container; Croquette (1989*a*, *b*) has shown that only above about 28 rolls do the predicted and observed Rayleigh numbers for instability onset show good agreement.

5. Conclusions

SMC is interesting for at least two reasons: first, because it is a system which can closely approximate RBC but has the remarkable Prandtl number range $0.04 \leqslant Pr \leqslant 1.5$; and second, because SMC can be made to deviate from RBC in a controlled way, providing a novel and completely different form of convection. The former gives SMC the potential to be an extremely valuable tool for understanding convective flows, but the extent of the superfluid corrections must first be determined and understood.

We find that both Ra_c and q_c are affected by superfluid effects, and the calculation of Ra_c in terms of the layer height suggests a direct method for quantitative determination of the superfluid effects in terms of the superfluid dissipation length scale $\lambda_\circ$. We have built a variable aspect ratio convection apparatus and have measured $\lambda_\circ$ as a function of temperature.

Whether or not SMC is well approximated by the Boussinesq equations depends on the ratio $\lambda_\circ/d$. When it is less than $\approx 10^{-1}$, superfluid effects induce small shifts in Ra_c and q_c due to the reduced buoyancy but otherwise do nothing. In this case we conclude that SMC well approximates RBC near onset. As $\lambda_\circ/d$ increases above 10^{-1} though, the superfluid effects rapidly stabilize the layer heated from above and damp out convection altogether. In this case SMC does not approximate RBC with ideal conducting boundaries. Experimentally, the condition $d \gg \lambda_\circ$ is easily realized for all but the shortest of cell heights, so that superfluid effects in SMC are normally negligible at the onset of convection.

The situation far above onset is less certain. As there are no calculations available for the SMC nonlinear states, a similar coupled theoretical–experimental approach for quantifying superfluid effects above onset is not at present possible. Additional experimental and theoretical work is required to better characterize superfluid effects on the convective flows well above onset. However, from comparison of measured

SMC nonlinear instability properties with predictions of RBC calculations – in particular oscillatory instability frequencies and the location of the codimension-2 point – we may with some confidence conclude that the SMC–RBC analogy also holds reasonably well up to the level of the secondary instabilities. The experimental evidence suggests that departures of SMC from the Boussinesq equations are no stronger than finite aspect ratio effects, and thus SMC remains well suited to the study of nonlinear instabilities. A survey of novel low-*Pr* instabilities is the subject of Part 2.

This work has been supported by the NSF under grants DMR–9017236 and DMR–9321791.

REFERENCES

AHLERS, G. 1974 Low-temperature studies of the Rayleigh-Bénard instability and turbulence. *Phys. Rev. Lett.* **33**, 1185–1188.

AHLERS, G. 1975 The Rayleigh-Bénard instability at helium temperatures. In *Fluctuations, Instabilities, and Phase Transitions* (ed. T. Riste), pp. 181-193. Plenum.

AHLERS, G. 1989 Experiments on bifurcations and one-dimensional patterns in nonlinear systems far from equilibrium. In *Lectures in the Sciences of Complexity* (ed. D. L. Stein). Addison-Wesley.

AHLERS, G. & DUNCAN, R. V. 1988 Finite-size effects on the thermal conductivity of ^{4}He near the superfluid transition. *Phys. Rev. Lett.* **61**, 846–848.

BEHRINGER, R. P. 1985 Rayleigh-Bénard convection and turbulence in liquid helium. *Rev. Mod. Phys.* **57**, 657–687.

BEHRINGER, R. P. & AHLERS, G. 1982 Heat transport and temporal evolution of fluid flow near the Rayleigh-Bénard instability in cylindrical containers. *J. Fluid Mech.* **125**, 219–258.

BOLTON, E. W., BUSSE, F. H. & CLEVER, R. M. 1986 Oscillatory instabilities of convection rolls at intermediate Prandtl number. *J. Fluid Mech.* **164**, 469–485.

BUSSE, F. H. 1981 Transition to turbulence in Rayleigh-Bénard convection. In *Hydrodynamic Instabilities and the Transition to Turbulence* (ed. H. L. Swinney and J. P. Gollub), pp. 97–137. Springer.

BUSSE, F. H. & CLEVER, R. M. 1979 Instabilities of convection rolls in a fluid of moderate Prandtl number. *J. Fluid Mech.* **91**, 319–335.

CHANDRASEKHAR, S. 1961 *Hydrodynamic and Hydromagnetic Stability.* Dover.

CHIFFAUDEL, A., PERRIN, B. & FAUVE, S. 1989 Spatiotemporal dynamics of oscillatory convection at low Prandtl number: waves and defects. *Phys. Rev.* A **39**, 2761–2764.

CLEVER, R. M. & BUSSE, F. H. 1974 Transition to time-dependent convection. *J. Fluid Mech.* **65**, 625–645.

CLEVER, R. M. & BUSSE, F. H. 1978 Large wavelength convection rolls in low Prandtl number fluids. *Z. Angew. Math. Phys.* **29**, 711–714.

CLEVER, R. M. & BUSSE, F. H. 1987 Nonlinear oscillatory convection. *J. Fluid Mech.* **176**, 403–417.

CROQUETTE, V. 1989*a* Convective pattern dynamics at low Prandtl number: Part I. *Contemp. Phys.* **30**, 113–133.

CROQUETTE, V. 1989*b* Convective pattern dynamics at low Prandtl number: Part II. *Contemp. Phys.* **30**, 153–171.

CROSS, M. C. 1980 Derivation of the amplitude equation at the Rayleigh-Bénard instability. *Phys. Fluids* **23**, 1727–1731.

CROSS, M. C. & HOHENBERG, P. C. 1993 Pattern formation outside of equilibrium. *Rev. Mod. Phys.* **65**, 851–1112.

DEISSLER, R. J., ECKE, R. E. & HAUCKE, H. 1987 Universal scaling and transient behaviour of temporal modes near a Hopf bifurcation. *Phys. Rev.* A **36**, 4390–4401.

DELONG, L. E., SYMKO, O. G. & WHEATLEY, J. C. 1971 Continuously operating ^{4}He evapouration refrigerator. *Rev. Sci. Instrum.* **42**, 147–150.

ECKE, R. E., HAUCKE, H., MAENO, Y. & WHEATLEY, J. C. 1986 Critical dynamics at a Hopf bifurcation to oscillatory Rayleigh-Bénard convection. *Phys. Rev.* A **33**, 1870–1878.

FETTER, A. L. 1982*a* Onset of convection in dilute superfluid ^{3}He–^{4}He mixtures: Unbounded slab. *Phys. Rev.* B **26**, 1164–1173.

FETTER, A. L. 1982*b* Onset of convection in dilute superfluid ^{3}He–^{4}He mixtures: Closed cylindrical container. *Phys. Rev.* B **26**, 1174–1181.

GAO, H., METCALFE, G., JUNG, T. & BEHRINGER, R. P. 1987 Heat-flow experiments in liquid ^{4}He with a variable cylindrical geometry. *J. Fluid Mech.* **174**, 209–231.

HAUCKE, H., MAENO, Y., WARKENTIN, P. A. & WHEATLEY, J. C. 1981 Time-dependent thermal convection in dilute solutions of ^{3}He in superfluid ^{4}He. *J. Low Temp. Phys.* **44**, 505–533.

KHALATNIKOV, I. M. 1965 *An Introduction to the Theory of Superfluidity.* W. A. Benjamin.

KOLODNER, P., WALDEN, R., PASSNER, A. & SURKO, C. M. 1986 Rayleigh-Bénard convection in an intermediate-aspect-ratio container. *J. Fluid Mech* **163**, 195–226.

LANDAU, L. 1941 The theory of superfluidity of helium-II. *J. Phys. USSR* **5**, 71–90.

LIBCHABER, A., FAUVE, S. & LAROCHE, C. 1983 Two-parameter study of the routes to chaos. *Physica* **7D**, 73–84.

LIPA, J. A. & CHUI, T. C. P. 1987 High-resolution thermal-conductivity measurements near the lambda point of helium. *Phys. Rev. Lett.* **58**, 1340–1343.

LONDON, F. 1954 *Superfluids: Macroscopic Theory of Superfluid Helium.* Dover.

MAENO, Y., HAUCKE, H., ECKE, R. E. & WHEATLEY, J. C. 1985 Oscillatory convection in a dilute ^{3}He-superfluid-^{4}He solution. *J. Low Temp. Phys.* **59**, 305–345.

MAINIERI, R., SULLIVAN, T. S. & ECKE, R. E. 1989 Two-parameter study of the quasiperiodic route to chaos in convecting ^{3}He-superfluid-^{4}He mixtures. *Phys. Rev. Lett.* **63**, 2357–2360.

MANNEVILLE, P. 1990 *Dissipative structures and Weak Turbulence.* Academic Press.

METCALFE, G. 1991 Using superfluid mixtures to probe convective instabilities. PhD thesis, Duke University.

METCALFE, G. & BEHRINGER, R. P. 1993 Superfluid effects at the onset of convection in ^{3}He-superfluid-^{4}He mixtures. *J. Low Temp. Phys.* **90**, 95–117.

METCALFE, G. & BEHRINGER, R. P. 1996 Convection in ^{3}He–superfluid-^{4}He mixtures. Part 2. A survey of instabilities. *J. Fluid Mech.* **307**, 297–331.

MOTSAY, R. W., ANDERSON, K. E. & BEHRINGER, R. P 1988 The onset of convection and turbulence in rectangular layers of normal liquid ^{4}He. *J. Fluid Mech.* **189**, 263–286.

NEWELL, A. C., PASSOT, T. & SOULI, M. 1990 The phase diffusion and mean drift equations for convection at finite Rayleigh numbers in large containers. *J. Fluid Mech.* **220**, 187–252.

PARSHIN, A. YA. 1969 Internal gravitational waves in a superfluid solution. *JETP Lett.* **10/12**, 362–364.

POCHEAU, A. 1988 Transition to turbulence of convective flows in a cylindrical container. *J. Phys. (Paris)* **49**, 1127–1145.

POLLACK, G. L. 1969 Kaptiza resistance. *Rev. Mod. Phys.* **41**, 48–81.

STEINBERG, V. 1981*a* Stationary convective instability in a superfluid ^{3}He–^{4}He mixture. *Phys. Rev.* A **24**, 975–987.

STEINBERG, V. 1981*b* Oscillatory convective instability in a superfluid ^{3}He–^{4}He mixture. *Phys. Rev.* A **24**, 2584–2594.

SULLIVAN, T., ECKE, R. E. & STEINBERG, V. 1991 Superfluid mixture shadowgraph calculation. In *Proc. 8th Annual University of Oregon Conference* (ed. R.J. Donnelly).

WALDEN, R. D., KOLODNER, P., PASSNER, A. & SURKO, C. M. 1987 Heat transport by Parallel-roll convection in a rectangular container. *J. Fluid Mech.* **185**, 205–234.

WARKENTIN, P. A., HAUCKE, H. J., LUCAS, P. & WHEATLEY, J. C. 1980 Stationary convection in dilute solutions of ^{3}He in Superfluid ^{4}He. *Proc. Natl Acad. Sci. USA* **77**, 6983–6987.